Chapter 24
Tailoring Spins and Orbitals in Spin–Orbitronic Interfaces Probed by X-Ray Magnetic Circular Dichroism

Jun Okabayashi

Abstract This review summarizes recent X-ray magnetic circular dichroism (XMCD) studies for interfacial perpendicular magnetic anisotropy. The nature of chemical bonding and electron occupancies bring novel properties at the interfaces. The control of orbital magnetic moments could enable to reveal and utilize novel promising phenomena beyond spintronics. Detailed investigations of anisotropic orbital magnetic moments at the interfaces in Fe|MgO and Co|Pd cases are discussed with brief introduction of theoretical background of XMCD spectra and brief history of this technique.

24.1   Introduction

Magneto-optics has been developed to investigate electronic and magnetic states. Linearly polarized light passes through transient magnets leading to an output of circularly polarized lights, referred to as Faraday effect. In case of a reflection geometry, similar effects are observed as Kerr effect. These effects originate from the difference in absorption coefficients between right- and left-circularly polarized lights, leading to magnetic circular dichroism (MCD). For the incident beam, the ultraviolet region has been utilized. Since the development of synchrotron radiation, in particular, circularly polarized beams in the soft- and hard-X-ray regions, magneto-optical techniques with MCD using circularly polarized X-rays have been extensively developed, referred to as XMCD techniques.

We summarize the history of XMCD. Erskine and Stern theoretically predicted the Ni-M-edge XMCD through the off-diagonal parts of the conductivity tensor σ_{xy}, which is 10^{-1} of the diagonal part σ_{xx} [1]. In 1987, Schütz et al. experimentally observed the XMCD of the Fe K-edge [2]. Using soft X-rays, Chen et al. succeeded in the measurements of XMCD of Ni L-edges [3]. Theoretical investigations of XMCD have also been proceeded with the experimental developments. Selection rules for

J. Okabayashi (✉)
Research Center for Spectrochemistry, The University of Tokyo, Hongo 7-3-1, Bunkyo, Tokyo 113-0033, Japan
e-mail: jun@chem.s.u-tokyo.ac.jp

optical absorption permit a difference of quantum numbers of $\Delta l = \pm 1$, which corresponds to an excitation from p to d states in transition-metal (TM) compounds. For $3d$ TMs, the L-edge absorption energies are located at the soft-X-ray regions. Magneto-optical sum rules, proposed by Carra and Thole, enabled quantitative estimations of spin and orbital magnetic moments [4, 5]. In 1995, C. T. Chen et al. reported conventional methods for the estimations of spin and orbital magnetic moments from sum rules using Fe and Co layers [6]. XMCD and its spectral analysis using sum rules became one of the standard techniques to deduce element-specific magnetic properties. In 1998, Koide et al. investigated the angular dependence of XMCD in order to reveal the magnetic anisotropy [7]. As the investigations of magnetic anisotropy were limited to phenomenological studies using magnetization measurements, studies from the point of view of electronic structure were required. The angular dependence in XMCD provides information about the anisotropy in spins and orbitals; it becomes a powerful technique to investigate the element-specific magnetic properties, particularly in layered interfacial structures [8]. After 2000, XMCD techniques have been continuously extended and combined with other techniques, which led to the development of XMCD microscopy [9] and time-resolved measurements [10].

A schematic of the XMCD beam-line is shown in Fig. 24.1. Soft X-rays in the range of 50–1,200 eV can be utilized for X-ray absorption spectroscopy (XAS), XMCD, and photoemission spectroscopy; the setup is constructed at the BL-7A, Photon Factory, High-Energy Accelerator Research Organization (KEK) in Tsukuba, Japan [11]. For XMCD, a 1.2-T electromagnet has been installed at the end station. As the beam comes from the bending magnets, circularly polarized lights for XMCD are obtained using the edges from the beam center, which is adjusted by a mirror in the beam-line. The beam and magnetic-field directions are fixed to be parallel, and the sample surface normal direction is rotated for the angular-dependent XMCD. Total-electron-yield (TEY) modes, which detect the drain currents excited from the sample at 3 nm from the sample surface, are utilized for XMCD measurements. In addition to TEY measurements, fluorescent yield modes are also employed, which probe to a depth of approximately 100 nm from the sample surface.
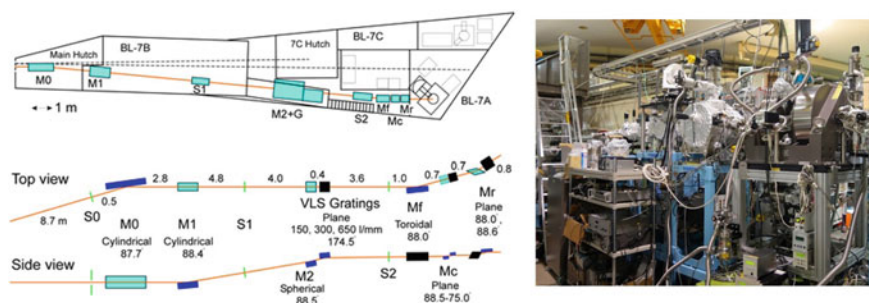
Fig. 24.1 Illustration of a beam-line and photograph of the end station

Fig. 24.2 Energy diagram considering the spin–orbit coupling in 3d states. The numbers in circles are transition probabilities from 2p to 3d states dependent on the quantum numbers
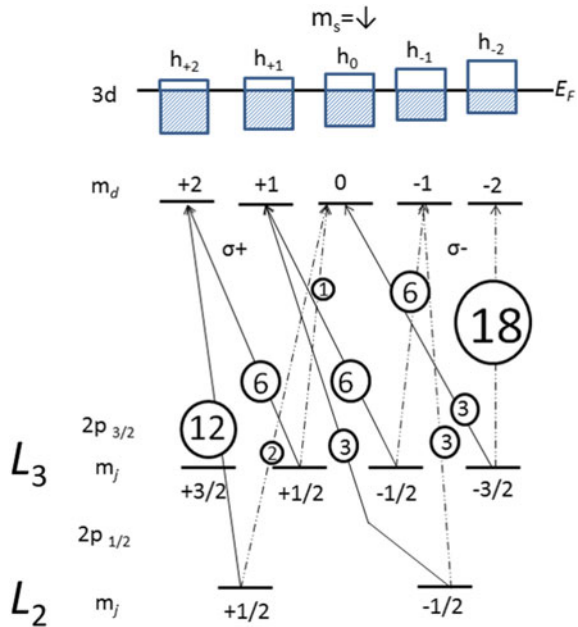
As XMCD analysis methods, magneto-optical sum rules for spin and orbital magnetic moments were established. These methods are summarized here. In particular, we focus on the magnetism in 3d TMs. As shown in Fig. 24.2, 3d states are split to up and down states by exchange interaction. Considering the spin–orbit interaction, the optical transition probabilities from 2p to 3d states are proportional to the Clebsch–Gordan coefficients. Un-occupancies of d states can be expressed as hole numbers h_{+2}, h_{+1}, h_0, h_{-1}, and h_{-2} for the five states. Estimated values of spin and orbital angular momenta can be defined as:

$$\langle L \rangle = -(2h_{+2} + h_{+1} + 0h_0 - h_{-1} - 2h_{-2})\hbar$$
$$\langle S \rangle = -(h_{+2} + h_{+1} + h_0 + h_{-1} + h_{-2})\hbar/2.$$

Using the coefficients in Fig. 24.2, the excitations by circularly polarized lights are estimated as:

$$L_3 : \Delta I_{L3} \propto 6h_{+2} + 6h_{+1} + 3h_0 - 6h_{-1} - 18h_{-2}$$
$$L_2 : \Delta I_{L2} \propto 12h_{+2} + 3h_{+1} - 2h_{-1} - 3h_{-2}.$$

Therefore, a total summation leads to:

$$\Delta I_{L3} + \Delta I_{L2} \propto 9(2h_{+2} + h_{+1} - h_{-1} - 2h_{-2}) \propto 9\langle L \rangle.$$

If the intensities of ΔI_{L3} and ΔI_{L2} are equal with different signs, the orbital angular momentum becomes quenched. $\langle S \rangle$ cannot be explicitly deduced from the XMCD; it can be expressed using the higher orders in the multipole expansion. The second order is the magnetic dipole term m_T, which exhibits the effect of spin anisotropy through the tensor Q_{ij}. The relation $m_T = \sum_\beta Q_{\alpha\beta} S_\alpha$ is satisfied [12]. The m_T term does not become negligible in symmetry-broken surfaces and interfaces. In highly symmetric crystals, m_T can be negligible. Based on these considerations, the sum rules can be expressed as:

$$m_{\text{orb}} = -\frac{4}{3}\left[\frac{\Delta I_{L3} + \Delta I_{L2}}{I_{L3} + I_{L2}}\right] n_h$$
$$m_{\text{spin}} - 7m_T = -2\left[\frac{\Delta I_{L3} - 2\Delta I_{L2}}{I_{L3} + I_{L2}}\right] n_h$$

in a unit of μ_B. In an anisotropic system, such as interfaces, the in-plane and out-of-plane directions are separately described as $m_{\text{orb}}^\perp$, $m_{\text{orb}}^\parallel$, $m_T^\perp$, and $m_T^\parallel$. Considering the relationship: $m_T^x + m_T^y + m_T^z = 0$, the m_T in the in-plane and out-of-plane directions are related by:

$$m_T^\perp + 2m_T^\parallel = 0$$

Further, the angular dependences of m_{orb} and m_T are expressed as:

$$m_{\text{orb}}^\theta = m_{\text{orb}}^\perp \cos^2\theta + m_{\text{orb}}^\parallel \sin^2\theta$$
$$m_T^\theta = m_T^\perp \cos^2\theta + m_T^\parallel \sin^2\theta$$

Using these five equations, the five values of m_{spin}, $m_{\text{orb}}^\perp$, $m_{\text{orb}}^\parallel$, $m_T^\perp$, and $m_T^\parallel$ are deduced. In particular, in the special case of magic angle obtained by: $3\cos^2\theta - 1 = 0$, $m_T^\theta = -m_T^\parallel(3\cos^2\theta - 1) = 0$ can be obtained in the geometry of $\theta = 54.7°$.

Using the above considerations, the element-specific spin and orbital magnetic moments are estimated quantitatively from the XMCD line-shape analyses. In this Chapter, possible origins of novel properties deduced from XMCD analyses are introduced for some systems. Interfaces induce novel properties, not present in the bulk form. The control of the interface atomic structure paves the way for novel artificial material designs.

24.2 Importance of Spintronics and Spin-Orbitronics

In this section, I briefly explain the importance of spintronics, utilized in applications such as magneto-resistive random access memory (MRAM). The research field of spin-orbitronics has attracted recent interests regarding the control of the spin–orbit interaction at thin-film interfaces, which paves the way for a new research

field beyond spintronics. In order to fabricate functional high-performance devices, advanced material growth and understanding of the interfacial properties are required.

In the research field of spintronics, atomically controlled multilayered structures have been investigated, providing giant magnetoresistance (GMR) effects, discovered in Fe/Cr multilayers [13]. Prof. Fert and Prof. Grünberg were awarded with a Nobel prize in 2007 owing to the importance of the GMR effects, which accelerated the MRAM technology. Multilayers combining different types of elements exhibit novel properties beyond those in the bulk form. In particular, memory devices using magnetic states are employed in data storage. In order to improve the memory-device performances, the spin switching from the in-plane directions in the films is shifted to out-of-plane switching owing to the high densities in data storage technology. For this purpose, the perpendicular magnetic anisotropy (PMA) becomes important in the development of spintronic devices. However, the emergence of PMA in the bulk form requires non-symmetric distorted crystal structures such as spinel-type structures including oxides or alloys with Pt. Spins in $3d$ TMs and large spin–orbit coupling constants in $4d$ or $5d$ TMs combine at the film interfaces, providing PMA properties including out-of-plane magnetism of spins in $3d$ TMs and induced magnetism in heavy-metal elements. Extensive efforts have been devoted to fabricate atomically flat interfaces exhibiting PMA. Further, studies without using heavy-metal elements are important to develop low-cost memory devices. Recent studies have been focused on the control of spin–orbit interaction at interfaces, which brings novel properties for magnetization switching; e.g., spin–orbit torque could be employed for a low-power operation in the MRAM technology. Therefore, precise measurements of interfacial electronic and magnetic properties are strongly desired.

Spin-orbitronics is a novel research field, emerging after the advancements in electronics and spintronics. Figure 24.3 shows a comparison between electronics, spintronics, and orbitronics. Electronics involves the control of electrons, with devices such as transistors. The conjugate field is the electric field. In spintronics, developed by an analogy of electronics using electron spins, spins are controlled. The magnetic field is considered as the conjugate field. On the other hand, orbitronics involves a control of orbital states in the same manner [14]. Orbital states are controlled by the electron occupancies of $3d$ states, as shown in Fig. 24.2, which can be detected by XMCD. However, unlike electrons or spins, the orbital moments cannot be easily understood. Modulation of orbital occupancies is achieved by controlling lattice distortion, crystal field, or external electric field. Therefore, symmetry-broken interfaces with different types of elements are a promising platform to develop orbitronic systems.

Several phenomena have been revealed using element-specific characterizations, as illustrated in Fig. 24.4. "Induced magnetism" in non-magnetic elements can be detected by XMCD. Orbital magnetism can also be detected by XMCD; the orbital moment anisotropy is crucial at film interfaces [15]. Exchange coupling phenomena are clearly detected; ferromagnetic and antiferromagnetic types of coupling can be analyzed [16]. Orbital ordering through spin–orbit coupling is also related to the orbital magnetic moments, and can be detected by XMCD [17]. In addition, the orbital ordering is related to lattice distortions. Both structural and electronic properties have
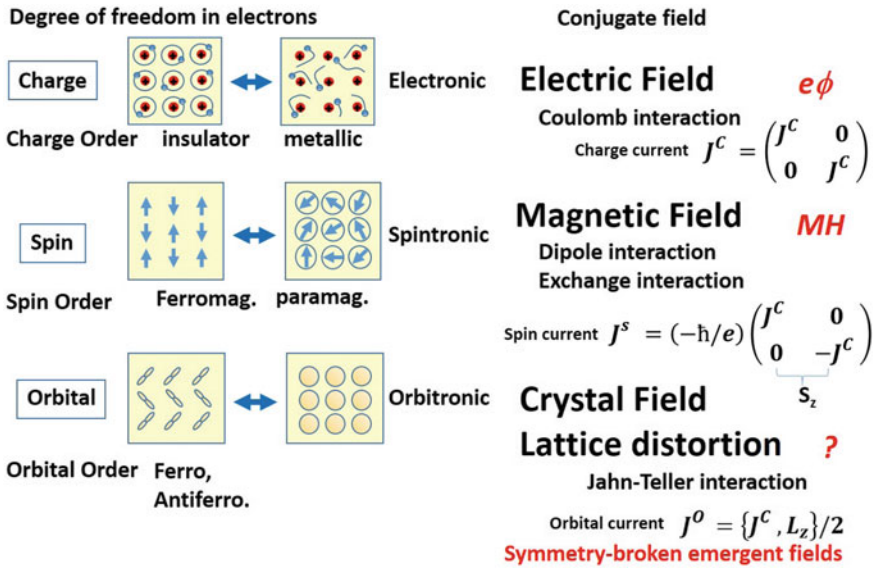
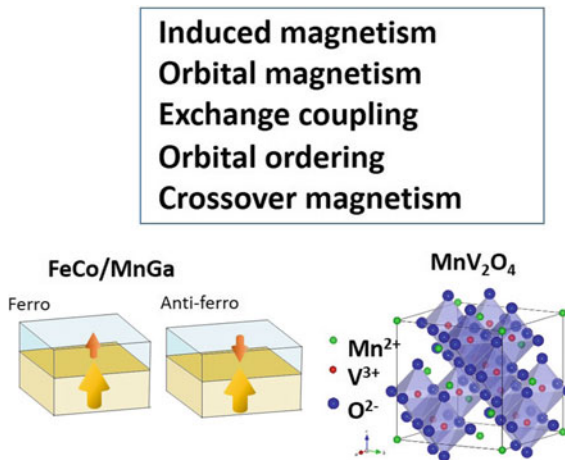**Fig. 24.3** Comparison of electronics, spintronics, and orbitronics

Fig. 24.4 Investigation of novel spin-orbitronic phenomena using XMCD [16, 17]

to be investigated explicitly. In addition, for spinel-type or perovskite-type transition-metal (TM) oxides, the control of crystal fields has been demonstrated.

Considering the above potentials, XMCD-related investigations are discussed in the following sections: (1) PMA at Fe/MgO interface and (2) possible origin of the PMA in Co/Pd multilayers.

## 24.3 Interfacial PMA in Fe/MgO Probed by XMCD[1]

Since the discovery of large tunnel magnetoresistance in single-crystal MgO-based magnetic tunnel junctions, the interfaces between MgO and magnetic layers have been investigated thoroughly [18]. Recently, large PMA energies of 0.21 MJ/m^3 have been developed by utilizing the interfaces between MgO and CoFeB transition metal alloys that are comparable to the perpendicular magnetic anisotropy (PMA) in Co/Pt multilayers without using heavy-metal elements [19]. This finding has initiated the development of high-performance MRAM using the interface PMA. For a fundamental understanding of the induction of PMA at the interface between a ferromagnetic layer and a MgO barrier layer, the electronic and magnetic structure of the interface between an ultrathin Fe layer and MgO must be clarified explicitly. Density functional theory (DFT) calculations revealed that a larger PMA appears at the interface between Fe and MgO than that of Co/MgO interfaces because of the difference in 3d orbital occupancies [20]. It has also been reported that the oxygen stoichiometry at the interface between Fe and MgO strongly depends on the PMA energies; namely, the over- and under-oxidization at the interface reduces the PMA. Experimentally, Koo et al. found that the PMA energies depend on the interface conditions and are controllable by the post-annealing process at the ultrathin 0.7-nm-thick Fe/MgO interface [21]. The maximum interfacial PMA is reported as 2.0 mJ/m^2. The values of PMA are of the same order of magnitude as those estimated by theoretical calculations. In order to investigate the PMA energy (K_{eff} [unit in J/m^3]), it is necessary to evaluate microscopically the orbital magnetic moments along parallel and perpendicular directions to the surface. Spin-orbit coupling is an essential factor concerning the origin of the interface PMA.

Until now, the origin of the large PMA in Fe/MgO has not yet been established because of the necessity of a large saturation magnetic field along the hard magnetization axis. Angular-dependent XMCD enables us to deduce the anisotropic orbital magnetic moments and investigate the large PMA at the Fe/MgO interface. In particular, Fe/MgO systems with different annealing conditions, which give rise to different PMA values, can provide the interpretation of the relationship between anisotropic orbital magnetic moments and PMA energies. In this section, we discuss the anisotropic interface orbital magnetic moments of ultrathin Fe facing a MgO layer by using angular-dependent XMCD and the PMA energies deduced from the orbital magnetic moments.

Samples were grown by using an ultra-high vacuum electron-beam evaporation on MgO (001) substrates. The sample structures are shown in Fig. 24.5. After cleaning the MgO (001) substrate at 1000 °C, a 5-nm-thick MgO layer was deposited on the substrate at 450 °C and a 30-nm-thick Cr buffer layer at 150 °C. Subsequently, the annealing process was performed at 800 °C in order to prepare the flat surface. A 0.7-nm-thick Fe layer, which corresponds to 5 monolayers (MLs), was deposited on the Cr buffer layer at 150 °C and a MgO layer was also grown on the Fe layer at 150 °C.
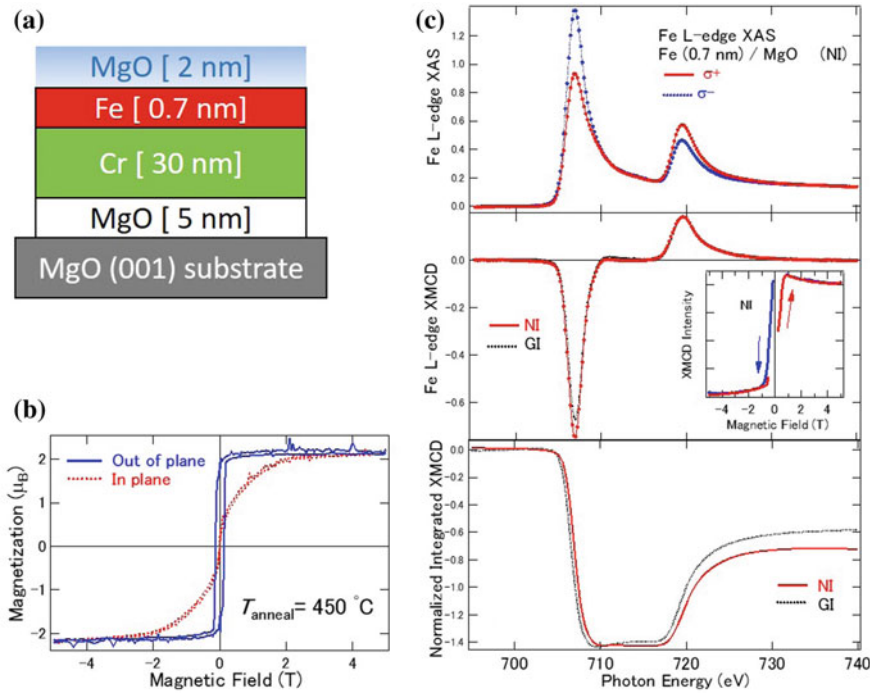
Fig. 24.5 a Sample structure with film thickness. **b** Magnetization curves measured by super-conductive quantum interference devices. **c** XAS, XMCD, and integrals of XMCD in NI and GI geometries [24]

After the deposition of the MgO capping layer, two kinds of samples prepared with the above conditions were post-annealed separately at 450 °C in order to enhance the PMA. Details of the surface and interface conditions and the fabrication procedures are reported in [21].

For XMCD measurements for Fe L-edges, magnetic fields (H_{ext}) of ± 5 T were applied using a superconducting magnet along the incident polarized soft X-rays in order to sufficiently saturate the magnetization along the direction of the magnetically hard axis. The total electron yield mode was adopted by detecting the drain currents from the samples. We changed the magnetic field directions in order to obtain right- and left-hand-side polarized X-rays while fixing the polarization direction of the incident X-ray. Angular-dependent XMCD was performed by rotating the angle between the incident beam and the direction of the sample's surface normal from the surface normal to 60°; these geometries are defined as normal incidence (NI) and grazing incidence (GI), respectively. In the case of the NI configuration, where both the photon helicity and the magnetic field directions are normal to the surface, the X-ray absorption processes involve the normal direction components of the orbital

angular momentum ($m_{orb}^{\perp}$). The GI configuration mainly allows the detection of only the in-plane orbital angular momentum components ($m_{orb}^{\parallel}$).

Figure 24.5 shows the XAS of a 0.7-nm-thick Fe/MgO interface after the annealing at 450 °C. The XMCD taken at the NI and GI geometries and the integrals of the Fe $L_{2,3}$ absorption edges XMCD spectra are also shown. Distinct metallic peaks are evident in the XAS of the Fe $L_{2,3}$-edges, which indicates that no atomically mixed layer formation with oxygen atoms occurred at the interface, even after the 450 °C annealing process. The XMCD spectra in the NI and GI setups display a distinct difference in the intensity between the L_3-edges while the L_2-edges show almost similar intensity. The measured XMCD signal for the Fe L_3-edge from the NI geometry was larger than that from the GI geometry, which suggests that the large orbital magnetic moments are induced when the H_{ext} is perpendicular to the film plane. The magneto-optical sum rule indicates that the integrated areas of both negative L_3 and positive L_2 peaks are proportional to the orbital magnetic moments. The residuals of the integrals of both L_3 and L_2-edges in the XMCD spectra are larger in the NI configuration than in the GI one, indicating that the large orbital magnetic moments remain in the NI setup. Bottom panel of Fig. 24.5 shows the integrated XMCD signals of the Fe L-edges for both NI and GI setups. A difference can be clearly observed in the residuals of the integrals for both L_3 and L_2 peaks. These integrated XMCD spectra indicate that the large orbital magnetic moments are enhanced in the NI geometry compared with those in GI one. This is reasonable for a Fe/MgO interface with a PMA related to the orbital magnetic moments.

Using the magneto-optical sum rules for the estimation of orbital and spin magnetic moments, we list the results with the NI and GI geometries in Table 24.1. The effective spin magnetic moments (m_s^{eff}) values were determined only from the GI geometry because the magic angle geometry of 57.3° from the surface normal can theoretically neglect the magnetic dipole terms. For the application of the sum rules, we assumed the hole numbers of the Fe $3d$ states to be 3.4 as a standard value of Fe bulk.[25] The results listed in Table 24.1 show that the orbital magnetic moments with $m_{orb}^{\perp}$ of 0.30 and $m_{orb}^{//}$ of 0.21 μ_B were calculated, where Δm_{orb} is defined as $\Delta m_{orb} = m_{orb}^{\perp} - m_{orb}^{//}$. Considering the Bruno relationship: $K \simeq (\xi/4)\,\alpha\,\Delta m_{orb}$, where ξ is the spin-orbit coupling constant, and α is the band-structure parameter, the PMA energies are proportional to Δm_{orb}. We obtained $K = 130$ µeV/atom, which corresponds to a PMA value of 1.48 mJ/m^2, assuming a Fe lattice constant of 0.287 nm with a body-centered-cubic structure facing the MgO at the interface.

Here, we discuss the origin of the PMA at the interface of Fe/MgO. Since the excitation processes in XMCD are regarded to be the atomic excitations from the core to unoccupied states, one can estimate the magnetic anisotropy energy per atom through the Bruno's relation by using the element-specific orbital magnetic moments. Since the diamagnetic and shape-anisotropic components of the magnetic anisotropy energy do not depend on the anisotropic orbital magnetic moments, the interface PMA values in units of J/m^2 were directly estimated. The contribution of K_{eff} should be calculated by using the diamagnetic components and the ultrathin Fe

Table 24.1 Spin and orbital magnetic moments estimated from the XMCD sum rules for Fe at the Fe/MgO interface. The in-plane ($m_{orb}^{\parallel}$) and out-of-plane ($m_{orb}^{\perp}$) components are listed in units of μ_B. The interfacial PMA amplitudes (K_i) obtained from XMCD in units of mJ/m^2 are also shown with those from SQUID. [24]

	$m_{orb}^{\perp}$ [μ_B]	$m_{orb}^{\parallel}$ [μ_B]
m_{spin} [μ_B]	–	2.08
m_{orb} [μ_B]	0.30	0.21
K_i^{XMCD}	1.48 mJ/m^2 (132 μeV/Fe)	
K_i^{VSM}	2.01 mJ/m^2	

layer thickness, which is the same process as the estimation of PMA values using DFT calculations.

Next, we discuss the PMA values obtained by XMCD and the comparison with other experimental and theoretical works reported in the literature. The DFT calculations determine a magneto-crystalline anisotropy energy of 0.2 meV/atom in a free-standing Fe with 1 ML in thickness, a value of 0.9 meV/atom at the Fe (1 ML)/MgO interface, and 1.5 meV/atom at the MgO/Fe (1ML)/MgO sandwiched structures [21]. These results suggest that the PMA of the Fe/MgO interface is enhanced with a double-facing interface. Considering that the obtained PMA value of 0.13 meV/(Fe atom) through the XMCD measurement for Fe (5 MLs)/MgO structure, the result is somewhat smaller than the estimated value from the DFT calculation (0.2 meV/Fe atom). It is noted that the value for $m_{orb}^{//}$ can be underestimated, because the angle for the X-ray incident in the NI configuration was not exactly parallel to the film plane i.e. 57.3°. Therefore, the PMA values can be estimated to be small relative to those from DFT calculations. Nevertheless, the estimated value of PMA through angular dependent XMCD for Fe (5 MLs)/MgO (001) structure, without an applied external electric field, was turned out to be comparable to that from the literature on the modulation of PMA by an electric field [22].

Considering the above results, the origin of PMA at the Fe/MgO interface can be described by the anisotropic orbital magnetic moments induced by the spin-orbit interaction at the interface. The anisotropic orbital magnetic moments, resulting from the modulation of the occupancies of the Fe 3d states at the interface, were obtained through the sum-rule analysis of the XMCD spectra. Figure 24.6 displays the schematic energy diagram of the Fe 3d states at the Fe/MgO interface. First, we discuss from the view point of molecular orbitals theory. The chemical bonding between Fe 3d_{z^2} and O 2p_z orbitals stabilizes the bonding states as shown in Fig. 24.6. Filling in these orbitals are not completely occupied, Fermi level locates near between these two atomic states. Second, interfacial electronic structures are discussed by ligand-field theory. The Fe 3d levels split into e$_g$ and t$_{2g}$ states due to the crystal field. At the surface or the interface accompanied with the symmetry breaking, the degenerated e$_g$ states of the $d_{x^2-y^2}$ and d_{z^2} orbitals split further because of the surface field and the hybridization with the O 2p_z orbital. The spin-orbit interaction induces further splitting depending on the direction of the $\boldsymbol{H}_{ext}$ and the magnetic quantum
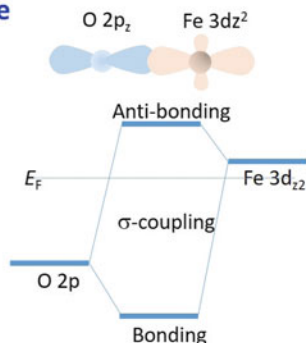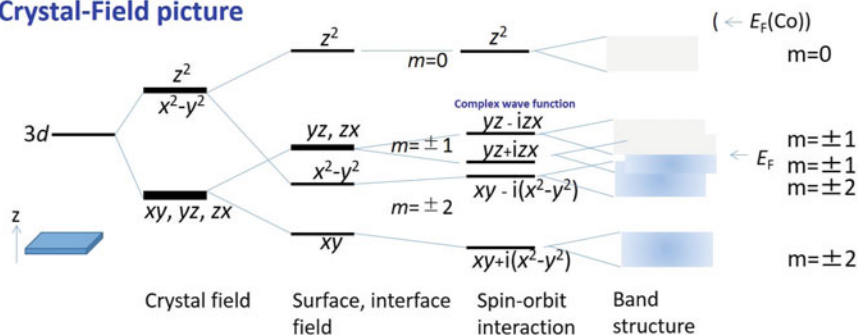
Fig. 24.6 Schematic diagrams in molecular-orbital scheme and ligand-field scheme for Fe $3d$ states

number m $(0, \pm 1, \pm 2)$. The d_{yz} and d_{zx} orbitals corresponding to $m = 1$ consist of the complex orbitals denoted as the d_{yz+izx} and d_{yz-izx} states. The anisotropy of charge occupancy between these complex states results in the anisotropic orbital magnetic moments. As was also indicated in the DFT calculations, the Fe $3d_z^2$ states are pushed up above the Fermi level through the hybridization with the O $2p_z$ orbital and the charge occupancies are modulated [20]. In addition, only when the H_{ext} perpendicular to the film plane, the modulation in the electron occupancies results in the enhanced $m_{orb}^{\perp}$. Therefore, due to the enhancement of $m_{orb}^{\perp}$ resulted from the spin orbit interaction and the hybridization between Fe $3d_{z^2}$ and O $2p_z$ orbitals, the large PMA can be expected for the Fe/MgO interface. It is well coincided with our XMCD results for the NI configuration, which showed enhanced $m_{orb}^{\perp}$. Note that the case of Co/MgO, Fermi level shifts to upper because of large charge number in $3d$ states, the gradation of orbital occupancies become small, resulting in the decrease of orbital moment enhancement.

In summary of this section, we have studied the interface PMA in ultrathin Fe/MgO (001) using angular-dependent XMCD. We found that the anisotropic orbital magnetic moments determined from the analysis of XMCD contribute to the large PMA energy, whose values depend on the annealing temperature. The large PMA ener-

gies deduced from the magnetization measurements are almost consistent with those estimated from the anisotropic orbital magnetic moments through the spin-orbit interaction. The enhancement of orbital magnetic moments can be explained by the hybridization between the Fe $3d_{z^2}$ and O $2p_z$ states at the Fe/MgO interface [23].

24.4 Interfacial Perpendicular Magnetic Anisotropy in Co/Pd Multilayers[2]

The interplay between $3d$ transition metals (TMs) and $4d$ or $5d$ TMs has been considered to offer opportunity of studying an interface-driven magnetic anisotropy with both spin and orbital degrees of freedom; namely the interplay between the two, the spin-orbit interaction through interfacial chemical bonding. Ultrathin Co/Pd multilayers are one of such representative artificial nanomaterials that exhibit *interface* perpendicular magnetic anisotropy (PMA), and the development of artificially synthesised PMA has led researchers to the expectation of ultra-high density recording media. Since then, extensive efforts have been made for studying electronic and spin structures of the interfaces of ultra-thin magnetic multilayers and nanostructures. Studies on Co atoms performed using XMCD have suggested the enhancement of orbital magnetic moments at the interfacial Co that is adjacent to Pd or Pt. It has been reported that the PMA emerges due to the cooperative effects between spin moments in $3d$ TMs and large spin-orbit interactions ξLS in the non-magnetic $4d$ or $5d$ TMs, where ξ is the spin-orbit coupling constants, L is orbital angular momentum, and S is the spin angular momentum. The Co/Pd interfaces and multilayers have also been employed to demonstrate the photo-induced precession of magnetisation [25, 26], the creation of skyrmions using the interfacial Dzyaloshinskii-Moriya interaction [27], and magnetisation reversal using the spin-orbit torque phenomena [28]. Despite the abovementioned careful studies and interesting trials with Co/Pd interfaces, the interfacial PMA, in particular the mechanism of *anisotropic* orbital magnetic moments, has not been fully understood for both Co and Pd sites. Bruno and van der Laan theoretically proposed an orbital moment anisotropy in $3d$ TMs within the second-order perturbation of the spin-orbit interaction (the weak coupling) for more than half-occupied electrons [29, 30]. However, in the case of strong spin-orbit coupling in $4d$ or $5d$ TMs, the validity of this perturbative formula has been debated. In order to study the mechanisms of PMA in Co/Pd multilayers, the contributions of orbital magnetic moments in each element should be explicitly considered.

However, it is challenging to study the anisotropy of the orbital magnetic moments of both Co and Pd elements using one specific experiment, due to the challenges in detection of the induced magnetic moments, of Pd in particular. In this study, we aim to overcome the above experimental challenges using the x-ray photon energy region that is common for both Co and Pd. In other words, a single experiment is

---

[2]This section is partly reproduced from J. Okabayashi, Y. Miura, and H. Munekata, Scientific Reports **8**, 8303 (2018), in accordance with the Creative Commons Attribution (CC BY) license.

Fig. 24.7 **a** Stacked structures and **b** magnetic field dependence of the Co L_3-edge XMCD for a photon energy of 778.0 eV, in the NI and GI configurations. **c** L-edge XAS, XMCD, and XMCD integrals of the Co/Pd multilayers that exhibit PMA [31]
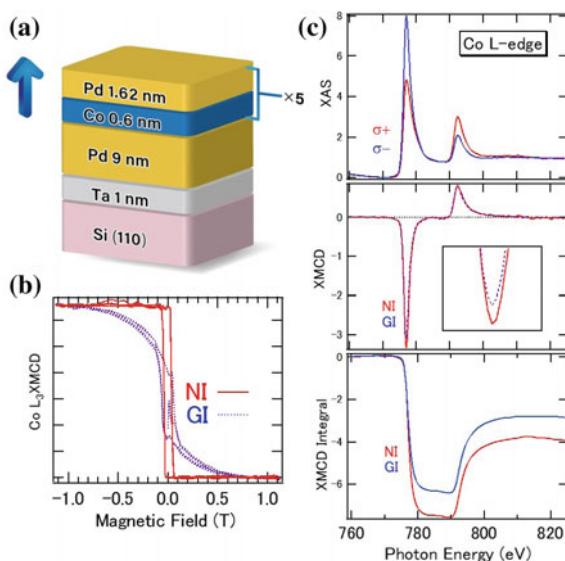
performed using the Pd $M_{2,3}$-edge absorption at ~530 eV, and Co $L_{2,3}$-edge absorption at ~770 eV taken by electron yield mode, instead of using different energy ranges for the Pd L-edges within 3.2 keV taken by fluorescence yield mode. The optical transitions from $2p$ to $3d$ states in $3d$ TMs, and those from $3p$ to $4d$ states in $4d$ TMs have the same transition probabilities. Therefore, the same transition processes could occur, even though the cross-section for the M-edges is smaller than that for L-edges. Furthermore, we adopt the angle-dependent XMCD that is a powerful experimental technique for studying anisotropic orbital magnetic moments. Taking into account that the X-ray absorption spectrum (XAS) attributed to the Pd $M_{2,3}$-edges ($3p$ to $4d$ transition) overlaps with that of the O K-edge absorption region, the surface oxide components have to be carefully removed, or the sample has to be prepared *in situ* in a detection chamber, in order to detect the Pd M-edge absorption signals. In this section, we have chosen the Ar-ion sputtering methods for surface cleaning. Experiments thus implemented lead us to the finding that the orbital magnetic moments in Co are anisotropic, whereas those in Pd are isotropic.

Ultrathin [Co/Pd]$_5$ multilayered structure grown by sputtering methods [25] was studied: Co (0.69 nm)/Pd (1.62 nm) that have PMA, which corresponds to four monolayers (MLs) of Co and eight MLs thickness of Pd. Cross-sectional transmission electron microscopy images have shown ⟨111⟩-oriented layered metallurgical structures with a good interface abruptness between Co and Pd [25]. Element-specific magnetisation hysteresis curves in normal incidence (NI) and oblique or grazing incidence (GI) geometries, taken at magic angle of 54.7° ($\cos^2\theta = 1/3$) from the sample surface normal, for Co are shown in Fig. 24.7. The photon energies are fixed at 778 eV for Co L_3-edge.

Table 24.2 The spin and orbital magnetic moments and magnetic dipole terms for perpendicular and in-plane directions in Sample A. The values are in the units of μ_B and are compared with the estimations from the XMCD and the first-principles density-functional-theory (DFT) calculations. Experimental error bars are estimated about 10% in Co and 20% in Pd for the applications of XMCD sum rules

	Co		Pd	
	XMCD	DFT	XMCD	DFT
$m_{\mathrm{spin}}^{\perp}$	1.82	1.87	0.25	0.31
$m_{\mathrm{spin}}^{\parallel}$	1.81	1.87	0.24	0.31
$7m_{\mathrm{T}}$	0.01	–	0.01	–
$m_{\mathrm{orb}}^{\perp}$	0.14	0.128	0.02	0.032
$m_{\mathrm{orb}}^{\parallel}$	0.11	0.096	0.02	0.033

Figure 24.7 shows the Co L-edge XAS and angular-dependent XMCD that exhibit PMA. The XMCD spectra for the NI and GI geometries, and the integrals of the Co $L_{2,3}$ absorption edges XMCD spectra, are shown in Fig. 24.7b and 24.7c, respectively. There are clear differences in XAS spectra, depending on the relative helicities of the incident beam. As the XAS spectra obtained from the NI and GI configurations are identical, only the XAS spectra in the NI configuration are shown. In Fig. 24.7b, the XMCD spectra for the NI and GI configurations show a distinct difference in intensity between the L_3-edges, while the L_2-edges have almost similar intensity profiles. The measured XMCD signal for the Co L_3-edge in the NI geometry was larger than that in the GI geometry when the effective field is perpendicular to the film plane. The magneto-optical sum rule indicates that the integrated areas of both negative L_3 and positive L_2 peaks are proportional to the orbital magnetic moments. The residuals of the integrals of both L_3 and L_2-edges in the XMCD spectra are larger in the NI configuration, compared to the GI configuration, which indicates that large orbital magnetic moments are observed for the NI configuration as shown in Fig. 24.7c. Assuming the Co hole number is 2.49 [6], we deduce that the orbital moments of the perpendicular and in-plane components for Sample A, $m_{\mathrm{orb}}^{\perp}$ and $m_{\mathrm{orb}}^{\parallel}$, are 0.14 μ_B and 0.10 μ_B, respectively. Note that the setup of $m_{\mathrm{orb}}^{\parallel}$ cannot detect the perfect in-plane contribution and almost half of $m_{\mathrm{orb}}^{\perp}$ and $m_{\mathrm{orb}}^{\parallel}$ are mixed which is proven by the MH curves in Co L_3-edge. Further, the spin magnetic moment (m_s) and magnetic dipole moment (m_T) of Co are 1.2 μ_B and 0.01 μ_B, respectively, with the uncertainties of $\pm$10%. These values are listed in Table 24.2 by comparing with those estimated from the DFT calculations.

Figures 24.8 show the XMCD signals of Sample A for the Pd M-edges, after the removal of surface contamination. The signals that emerge due to the O K-edge absorption are removed by the Ar ion sputtering, hence clear XMCD signals are observed. These signals are induced by the proximity effects with the Co layers. We note that the intensity scale of the Pd M-edge is two-orders of magnitude smaller than that of the Co L-edge, due to the difference in photo-ionisation cross-section. The Pd $M_{2,3}$-edge XAS line shapes exhibit satellite structures that appear at 542 and 567 eV,
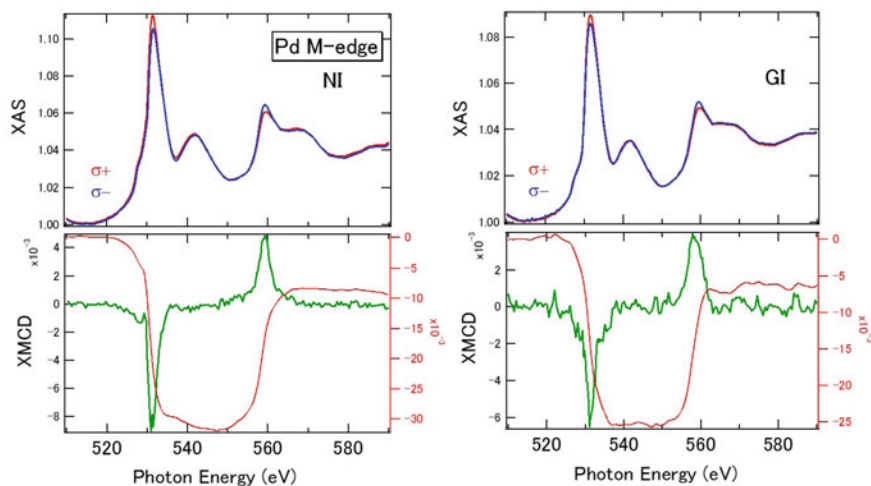
Fig. 24.8 *M*-edge XAS and XMCD of the Co/Pd multilayers that exhibit PMA. XAS at the NI configuration in left panel and the GI configuration at right panel. XMCDs acquired for the NI and GI configurations, respectively. The integrals of the XMCD are also plotted in the figures [31]

with higher photon energies of the main absorption peaks. They are obtained from the transitions from $3p$ to $5s$ states, and do not contribute to the XMCD signals. The Pd M-edge XMCD line shapes are almost identical in NI and GI setups, which suggests isotropic orbital moments in Pd, within the detection limits. Conventional magneto-optical sum rule analysis, often employed for $3d$ TMs (from $2p$ to $3d$ transition), can be applicable for the $3p$ to $4d$ transition in Pd M-edge XMCD with the same transition probabilities as that of the $2p$ to $3d$ transition. Assuming the hole number of the Pd $4d$ states is 1.10, for the NI configuration, the estimates of the spin and orbital magnetic moments are $0.25\,\mu_B$ and $0.02\,\mu_B$, respectively, with the error bars of $\pm 20\%$ because of the estimations of XAS spectral integrals include the ambiguities. In contrast to Co, the Pd XMCD line shapes remain almost unaffected in the angular dependence (within the detection limits). This indicates that the isotropic finite orbital moments in Pd do not directly contribute to the PMA.

We consider the (111) interfaces, as illustrated in Fig. 24.9a. The chemical bonding along the z-direction is staggered between Co and Pd, which causes the non-perfect σ bonding at the interface. Therefore, the isotropic distribution of orbital moments in Pd, and the anisotropic orbital moments in the Co layer at the interface promotes the PMA at the Co/Pd interface. On the other hand, it has been reported that the Pd (001) orientation cannot stabilise the PMA at the interface. Furthermore, three monolayers are necessary for the periodic stacking in (111) orientation, as shown in Fig. 24.9a. Therefore, (111) orientation stacks are necessary for the PMA, due to the tuning of the interfacial hybridisation strength.

In order to analyse the origin of the PMA, we computed the orbital moment anisotropy at each atomic site. Spin and orbital magnetic moments in Co and Pd
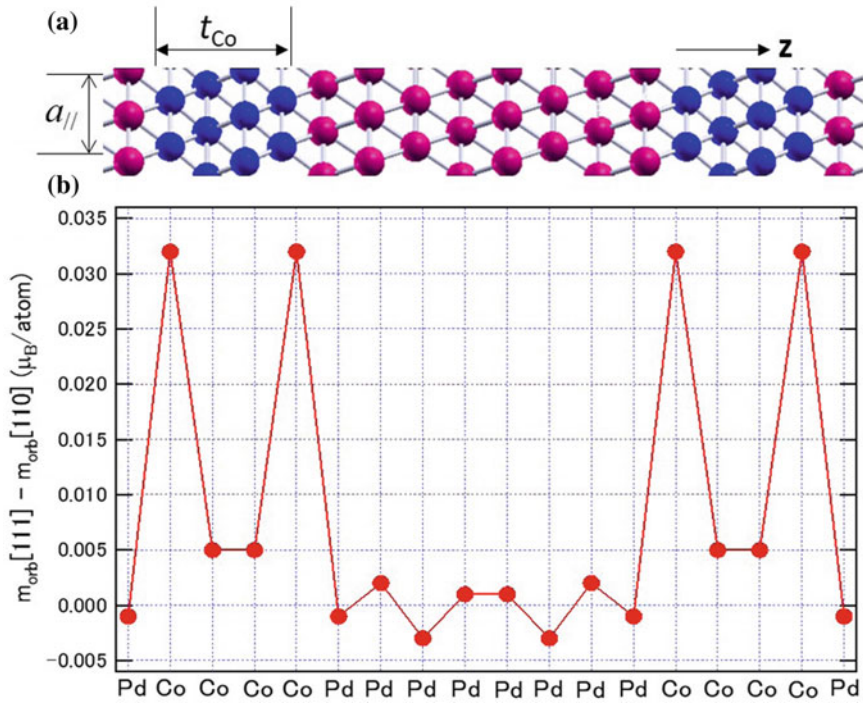
Fig. 24.9 **a** A schematic of the Pd(8ML)/Co(4ML)(111) multilayer. **b** Layer-resolved orbital moment anisotropy of the Pd(8ML)/Co(4ML), using $a_\parallel = 0.391$ nm, in DFT calculations [31]

sites are listed in Table 24.2. As shown in Fig. 24.9b, the orbital moment anisotropy of the Co atoms at the Co(4 ML)/Pd(8 ML) interfacial layer is enhanced and has a value of $0.033\ \mu_B$. We emphasise that the PMA of the Co monolayer that is next to the Pd monolayer can be augmented primarily by the contribution of the interfacial layer. The PMA in a Co monolayer decreases as the distance between this monolayer and the Co/Pd interface increases, which is expected due to the bulk-like Co-Co bonding. On the other hand, we estimate that the orbital moment anisotropy induced in Pd is very small compared with that in Co, even in the Pd layer that is next to Co (Fig. 24.9b). The induced magnetic moments in the Pd monolayer emerge due to the d-orbital hybridisation between neighboring Co $3d$ and Pd $4d$ states at the interface, which qualitatively coincides with the independence of orbital magnetic moment anisotropy in Pd sites deduced from the XMCD.

Figure 24.10a, b represent the contributions of the crystalline magnetic anisotropy on the anisotropy energy at each atomic site. Four types of spin transition processes occur between the occupied and unoccupied states within the second-order perturbation of the spin-orbit interaction. The "up-down" process implies a virtual excitation from an occupied up-spin state to an unoccupied down-spin state in the second-order perturbation. For Co sites, the transition between down-down spin states is dominant,

as shown in Fig. 24.10a. This suggests the conservation of spin states in the transition, which can be explained using the Bruno model assuming a large spin splitting. The Co sites exhibit positive energies in total, which confirms the orbital-moment-driven PMA. In contrast, for Pd, the spin-flipped transitions between up-down and down-up states become dominant due to the small band splitting, hence both spin-preserved and spin-flipped processes occur near the Fermi level. Element- and orbital-resolved density of states (DOS) for the Co $3d$ and Pd $4d$ states are shown in Fig. 24.10c and 24.10d, respectively. The DOS of both Co $3d(xy, x^2 - y^2)$ and $3d(yz, zx)$ orbitals at the interface contribute to the PMA because the $3d(xy, x^2 - y^2)$ and $3d(yz, zx)$ orbitals become dominant at the Fermi level in the minority-spin state. These states provide large matrix elements of L_z, $<3d(x^2 - y^2)\downarrow|L_z|3d(xy)\downarrow>$ and $<3d(yz)\downarrow|L_z|3d(zx)\downarrow>$, for the second order perturbation of the spin-orbit interaction, leading to an enhancement of the perpendicular components of the orbital magnetic moments. The DOS of the Co $3d$ states is clearly split, with a spin magnetic moment of 1.89 μ_B. We used the lattice constant of $a = 0.391$ nm for the equilibrium condition. The DOS of Pd $4d$ states is also split, due to the proximity with the Co layers, as shown in Fig. 24.10d. For the Pd $4d$ states, we estimated that the induced spin magnetic moment is 0.311 μ_B. The Pd $4d$ states exhibit a small splitting at the interfaces, whereas the DOS at the Fermi level is large, which is considered as a Stoner-type ferromagnetism. The matrix elements of $<4d(yz)\downarrow|L_z|4d(x^2 - y^2)\uparrow>$ are dominant in Pd sites, which favours to in-plane anisotropy. The spin-conserved transition in Co and spin-flipped transitions in Pd are illustrated in Fig. 24.10e. The enhancement of orbital moments of Co is explained by the spin conserved transition derived from the band structures. The spin-orbit coupling in heavy-metal elements causes a quadrupole-like formation by the spin-flip transitions, resulting in the magnetic dipole term (m_T), however it does not contribute to the anisotropy of the orbital moments. These results explain both the angular dependence of the Co L-edge and the Pd M-edge XMCD spectral line shapes.

Considering the results of XMCD and DFT calculations, we discuss the quadrupole-like contribution of the interfacial Pd layer. The spin sum rule includes not only the spin moment m_s, but also the magnetic dipole term m_T, and reveals the effective spin magnetic moment $m_s^{eff} = m_s + 7m_T$. Here, the m_T can be separated from the angular dependence of XMCD, as the GI configuration cancels out the m_T term for the magic angle geometry of 54.7° ($\cos^2\theta = 1/3$) with respect to the surface normal. Our Pd XMCD results indicate that the Pd orbital moments induced at the interface are isotropic. Note that m_T is an order of magnitude smaller than the orbital moments, i.e., 0.01 μ_B or less, comparable with the detectable limits. The element-specific PMA energy K that includes the m_T term beyond the Bruno model which is derived from only orbital moment anisotropy Δm_{orb} can be expressed theoretically as:

$$K \sim \frac{1}{4\mu_B}\xi \Delta m_{orb} - \frac{21}{2\mu_B}\frac{\xi^2}{\Delta_{ex}}\Delta m_T \tag{24.1}$$
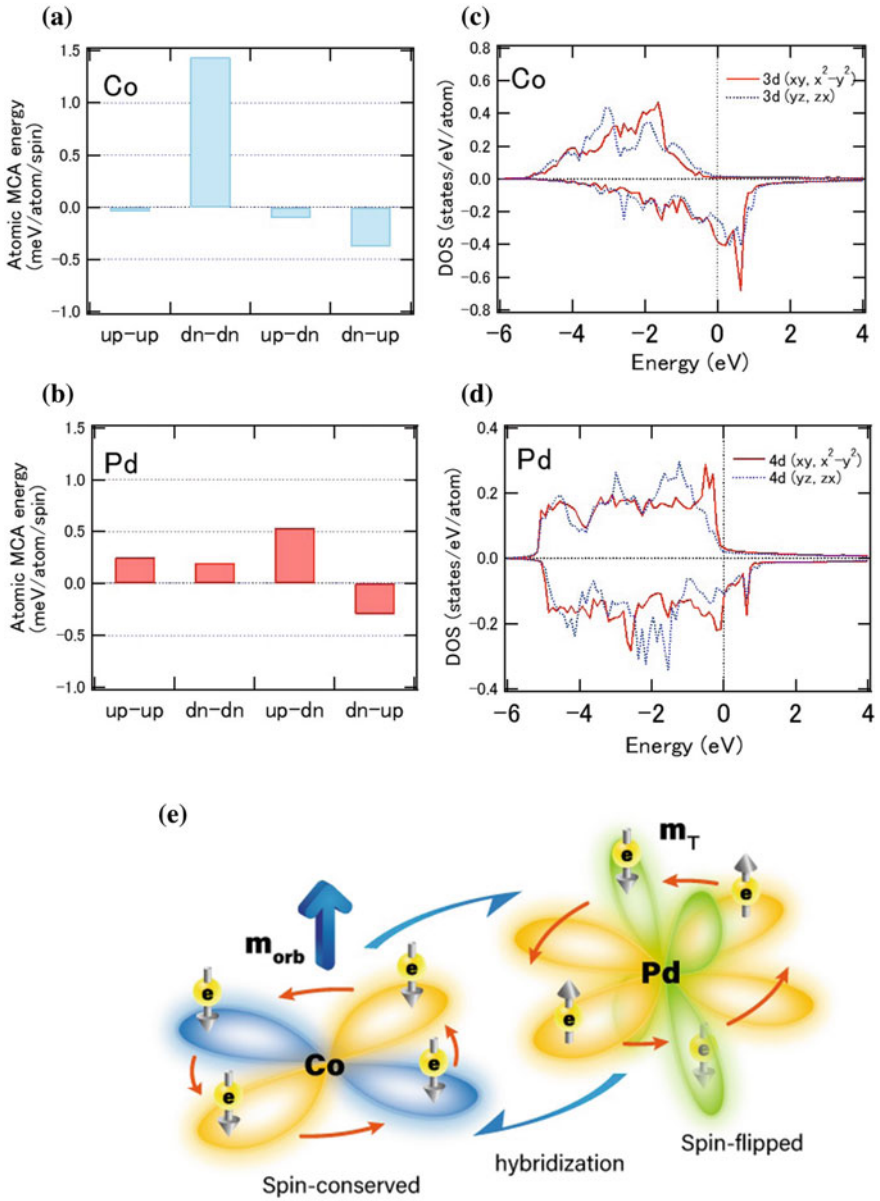
Fig. 24.10 Bar graph of the second-order perturbative contribution of the spin-orbit interaction to the MCA energy at the interfacial atomic sites of **a** Co and **b** Pd for the Pd(8ML)/Co(4ML), using $a_\parallel = 0.391$ nm. Spin-resolved local density of states (LDOS) of the $d(xy, x^2 - y^2)$ and $d(yz, zx)$ states for the interfacial **c** Co and **d** Pd sites, for the Pd(8ML)/Co(4ML), using $a_\parallel = 0.391$ nm. **e** A schematic of the electron hopping in Co and Pd at the interface. $3d(xy, x^2 - y^2)$ orbitals in Co and both Pd $4d(xy, x^2 - y^2)$ and $4d(yz, zx)$ orbitals are illustrated [31]

where Δ_{ex} is the exchange splitting between spin-up and spin-down bands. Δm_T satisfies the relation of $\Delta m_T = m_T^\perp - m_T^\parallel$ with $m_T^\perp = -2m_T^\parallel$. For Co, we estimate the first and second terms in (24.1) contributing 10^{-4} and 10^{-5} eV, respectively, in Co, assuming $\Delta_{ex\,Co} = 3$ eV, and $\xi_{Co} = 70$ meV, and the orbital moment anisotropy becomes dominant even in the finite m_T value. For Pd, the orbital anisotropy that corresponds to the first term becomes almost zero and the second term becomes dominant in the order of 10^{-4} eV because of small $\Delta_{ex\,Pd} = 200$ meV and large $\xi_{Pd} = 110$ meV, even if the m_T in Pd is as small as 0.01 μ_B. The relatively large spin-orbit coupling constant and small Pd exchange splitting contribute to the appearance of PMA by means of the second term in (24.1) with quadrupole-like interactions. The second term in Pd is comparable or smaller than the orbital moment anisotropy in Co. Therefore, the first term in (24.1) of orbital moment anisotropy in Co and the second term related to m_T in Pd contribute dominantly to E_{MCA} through the interfacial proximity effects. Furthermore, the contribution to the first term of (24.1) in Co is underestimated because Fig. 24.9b suggests the enhancement of Δm_{orb} at the interfacial layer. XMCD detects the signals from all layers, which suppresses the contribution from the interfacial layers. However, the enhancement of the orbital moment anisotropy can be concluded qualitatively.

Finally, we discuss the hybridization and spin-orbit coupling at the Co/Pd interfaces. Our findings indicate that the orbital moments in Pd are isotropic. This suggests that the magnetic dipole transitions can be essential, due to the mixing of spin-up and spin-down states in the Pd $4d$ states, even though the m_T values are much smaller than m_{orb}. As another physical origin of PMA, the facts that the radii of the Pd $4d$ orbitals are larger than those of Co $3d$ are also important, which results in the decrease of the anisotropy of the orbital moments and the increase of lattice strains. These effects couple at the interfaces, which enhances the PMA in Co/Pd multilayers. For relatively thick Co layers, the shape anisotropy in Co governs and suppress the effects of PMA at the interface, resulting in the in-plane anisotropy. The origin of PMA at the Co/Pd interface can be explained by the interfacial Co orbital moment anisotropy and spin-flipped processes at the Pd sites through the strong hybridization at Co/Pd interface, as illustrated by the magnetic dipoles in Fig. 24.10e.

In summary of this section, we have investigated the origin of PMA at Co/Pd interfaces using the angle–dependent XMCD and DFT calculations. The Co $3d$ orbital states are anisotropic, while the Pd $4d$ orbital states are isotropic. In contrast to the large spin splitting in Co $3d$ states, the induced spin splitting in Pd $4d$ states at the interface exhibits a combination of up and down spin transitions that accompany the quadrupole-like states in Pd. In other words, the anisotropy of the orbital moments in Co is enhanced at the interface through the proximity with Pd and orbital moment anisotropy is not induced in Pd even in the facing layer on Co.

24.5 Theory of Interfacial Perpendicular Magnetic Anisotropy

Considering the above mentioned cases of Fe/MgO and Co/Pd interfaces, the microscopic origin of interfacial PMA can be discussed using theoretical formulations. In the simple case, the anisotropy of orbital magnetic moments is proportional to PMA assuming the large exchange splitting between majority and minority bands. When the exchange splitting is small and mixing of up and down spin states, the spin-flipped contribution has to be formulated. Generally, the magnetocrystalline energy E_{MCA} can be the sum of the two contributions,

$$E_{MCA} \sim E^{\downarrow\downarrow}(\sigma) + E^{\uparrow\downarrow}(\sigma)$$

where $\downarrow\downarrow$ and $\uparrow\downarrow$ represent the spin transition of spin-conserved and spin-flipped cases, respectively. σ represents the directions of spins (x, y, and z). Spin-orbit interaction H_{SO} can be written as

$$H_{SO} = \xi\{1/2(l_+s_- + s_+l_-) + l_zs_z\}$$

by using ladder operators. The term of $l_+s_- + s_+l_-$ corresponds to the spin-flipped process. The l_zs_z term corresponds to the orbital moment anisotropy in spin-conserved state. Within the second-order perturbation of spin-orbit interaction, assuming the lattices elongated to z axis, E_{MCA} can be deduced by the comparison between out-of-plane and in-plane directions and formed as follows [32]:

$$E_{MCA} \sim -\frac{\xi}{4}(l_z - l_x) + \xi^2\frac{|\langle\downarrow|l_z|\uparrow\rangle|^2 - |\langle\downarrow|l_x|\uparrow\rangle|^2}{\Delta_{ex}} \qquad (24.2)$$

In this formulation, the cases of $l_z - l_x$ contributions become positive coefficients. Since $l_z^2 - l_x^2$ can be written to be $-1/2(l^2 - 3l_z^2)$, where $l^2 = l_x^2 + l_y^2 + l_z^2$, the second term is modified.

$$|E_{MCA}| \sim \frac{\xi}{4}|\Delta l_\uparrow - \Delta l_\downarrow| - \xi^2\frac{|\langle\downarrow|l^2 - 3l_z^2|\uparrow\rangle|}{2\Delta_{ex}} \qquad (24.3)$$

In this notation, positive amplitude of E_{MCA} stabilizes the PMA. Therefore, defining the quadrupole-like tensor formulation $T = l^2 - 3l_z^2$, the contribution from the second term become negative sign in the case of positive sign in the first term. Further, the matrix elements of second term in (24.3) are the connection between up and down states, suggesting that the mixing of majority and minority bands at the Fermi level is essential to enhance this term. While the first term is expressed as the anisotropy of orbital magnetic moments, the second term implies the changes of orbital shapes.

   In the case of negative T, the second term also favors the PMA. As the definition of $T_i = \sum_j Q_{ij}S_j$, $T < 0$ represents the spin quadrupole-like feature elongated to z-axis

with $3z^2 - r^2$-like prolate shape (cigar shaped along z-axis). On the other hand, $T > 0$ is defined as $x^2 - y^2$-like oblate type feature (donut shaped in xy plane). Because of the matrix elements of l_x in the spin-flipped transitions, magnetic quantum number has to change between ± 1 and ± 2 and between ± 1 and 0. Former transition exhibits the $3z^2 - r^2$-like prolate shape and later transition relates to $x^2 - y^2$-like oblate shape considering the shapes of wave functions. Beyond the orbital moment anisotropy, the second term is also the candidate of PMA. In order to enhance the second term, ξ must be large and Δ_{ex} be small. As discussed in Co/Pd interface, the m_T term in Pd 4d states contributes to PMA though large ξ and small Δ_{ex}. In the case of Fe/MgO case, ξ of Fe atom is as small as 50 meV and large exchange splitting, resulting in the negligible second term contribution. Therefore, the cases which second term becomes dominant are limited in the cases using heavy-metal elements which cooperate with 3d TMs through the orbital hybridization at the interfaces.

As for the comparison with the first-principles calculation and XMCD, it should be noted about the difference in the second term estimations. Above mentioned theoretical formulation of spin-flipped term can be estimated by the calculation as $E(\uparrow\downarrow)$ + $E(\downarrow\uparrow)$. However, in XMCD spin sum rule, the m_T term—$(21/2)$ $(\xi^2/\Delta_{ex})\Delta m_T$ written in the previous section includes not only spin-flipped term but also spin-conserved states in principles in the notation of $\{-2E(\downarrow\downarrow) - 2E(\uparrow\uparrow) + E(\uparrow\downarrow) + E(\downarrow\uparrow)\}$. As defined by van der Laan [30], the correction of spin-conserved term must be included when estimating the PMA energy.

24.6 Summary and Outlook in XMCD Spectroscopy

Recent XMCD studies were reviewed to clarify the PMA. The nature of chemical bonding and electron occupancies bring novel properties at interfaces. The control of orbital magnetic moments could enable to reveal and utilize novel promising phenomena beyond spintronics. As a next step, manipulation of orbital moments is required. For this purpose, the introduction of lattice strain by ferroelectric materials is a promising approach owing to the electric field control of strain in ferroelectric materials. Junctions between ferromagnets and ferroelectric materials introduce lattice strain into ferromagnets, and control the orbital moments reversibly by electric field. Another approach of analysis involving XMCD is to use microscopy with a high spatial resolution. In addition, not only element-specific but also spatial mapping of spins and orbitals are desired for interface spin-orbitronic analyses including topological properties.

Finally, for tailoring PMA at the interfaces, the enhancement of second term in (24.2) and (24.3) is essential. One of the interesting targets is $Mn_{3-x}Ga$. The Mn 3d orbital magnetic moments are almost quenched, resulting in no orbital moment anisotropy. Spin-flipped transitions become a key factor using even in small ξ in the distorted lattices. Therefore, the material designs of spin-orbitronics link to the modulation of lattice parameter, which opens up novel research fields in spin-orbitronics.

References

1. J.L. Erskine, E.A. Stern, Phys. Rev. B **12**, 5016 (1975)
2. G. Schütz, W. Wagner, W. Wilhelm, P. Kienle, R. Zeller, R. Frahm, G. Materlik, Phys. Rev. Lett. **58**, 737 (1987)
3. C.T. Chen, F. Sette, Y. Ma, S. Modesti, Phys. Rev. B **42**, 7262 (1990)
4. B.T. Thole, P. Carra, F. Sette, G. van der Laan, Phys. Rev. Lett. **68**, 1943 (1992)
5. B.T. Paolo Carra, M. Thole, M. Altarelli, X. Wang, Phys. Rev. Lett. **70**, 694 (1993)
6. C.T. Chen, Y.U. Idzerda, H.-J. Lin, N.V. Smith, G. Meigs, E. Chaban, G.H. Ho, E. Pellegrin, F. Sette, Phys. Rev. Lett. **75**, 152 (1995)
7. T. Koide, H. Miyauchi, J. Okamoto, T. Shidara, A. Fujimori, H. Fukutani, K. Amemiya, H. Takeshita, S. Yuasa, T. Katayama, Y. Suzuki, Phys. Rev. Lett. **87**, 257201 (2001)
8. J. Stöhr, J. Mag. Mag. Mater. **200**, 470 (1999)
9. J. Stöhr, H.C. Siegmann, Magetism, (Springer)
10. A. Kirilyuk, A.V. Kimel, T. Rasing, Rev. Mod. Phys. **82**, 2731 (2010)
11. K. Amemiya, H. Kondoh, T. Yokoyama, T. Ohta, J. Electron Spectrosc. Relat. Phenom. **124**, 151 (2002)
12. J. Stöhr, H. Konig, Phys. Rev. Lett. **75**, 3748 (1995)
13. G. Binasch, P. Grünberg, F. Saurenbach, W. Zinn, Phys. Rev. B **39**, 4828 (1989)
14. Y. Tokura, N. Nagaosa, Science **288**, 562 (2000)
15. J. Okabayashi, H. Sukegawa, Z. Wen, K. Inomata, S. Mitani, Appl. Phys. Lett. **103**, 102402 (2013)
16. J. Okabayashi, K.Z. Suzuki, S. Mizukami, J. Mag. Mag. Mater. **460**, 418 (2018)
17. J. Okabayashi, S. Miyasaka, K. Hemmi, K. Tanaka, S. Tajima, H. Wadati, A. Tanaka, Y. Takagi, T. Yokoyama, J. Phys. Soc. Jpn. **84**, 104703 (2015)
18. S. Yuasa, T. Nagahama, A. Fukushima, Y. Suzuki, K. Ando, Nat. Mater. **3**, 868 (2004)
19. S. Ikeda, K. Miura, H. Yamamoto, K. Mizunuma, H.D. Gan, M. Endo, S. Kanai, J. Hayakawa, F. Matsukura, H. Ohno, Nat. Mater. **9**, 721 (2010)
20. A. Hallal, H.X. Yang, B. Dieny, M. Chshiev, Phys. Rev. B **88**, 184423 (2013)
21. J.W. Koo, S. Mitani, T.T. Sasaki, H. Sukegawa, Z.C. Wen, T. Ohkubo, T. Niizeki, K. Inomata, K. Hono, Appl. Phys. Lett. **103**, 192401 (2013)
22. R. Shimabukuro, K. Nakamura, T. Akiyama, T. Ito, Physica E **42**, 1014 (2010)
23. K. Nakamura, T. Akiyama, T. Ito, M. Weinert, A.J. Freeman, Phys. Rev. B **81**, 220409R (2010)
24. J. Okabayashi, J.W. Koo, H. Sukegawa, S. Mitani, Y. Takagi, T. Yokoyama, Appl. Phys. Lett. **105**, 122408 (2014)
25. K. Yamamoto, T. Matsuda, K. Nishibayashi, Y. Kitamoto, H. Munekata, IEEE Trans. Magnet. **249**, 3155 (2013)
26. C. Boeglin, E. Beaurepaire, V. Halte, V. Lopez-Flores, C. Stamm, N. Pontius, H.A. Dürr, J.-Y. Bigot, Nature **465**, 458 (2010)
27. S.D. Pollard, J.A. Garlow, J. Yu, Z. Wang, Y. Zhu, H. Yang, Nature Commun. **8**, 14761 (2017)
28. M. Jamali, K. Narayanapillai, X. Qiu, L.M. Loong, A. Manchon, H. Yang, Phys. Rev. Lett. **111**, 246602 (2013)
29. P. Bruno, Phys. Rev. B **39**, 865 (1989)
30. G. van der Laan, J. Phys.: Condens. Matter **10**, 3239 (1998)
31. J. Okabayashi, Y. Miura, H. Munekata, Sci. Rep. **8**, 8303 (2018)
32. D. Wang, R. Wu, A.J. Freeman, Phys. Rev. B **47**(14), 932 (1993)